ADVANCED MATERIALS

Supporting Information

for *Adv. Mater.*, DOI: 10.1002/adma.201902250

Conductivity Tuning via Doping with Electron Donating and Withdrawing Molecules in Perovskite $CsPbI_3$ Nanocrystal Films

E. Ashley Gaulding, Ji Hao, Hyun Suk Kang, Elisa M. Miller, Severin N. Habisreutinger, Qian Zhao, Abhijit Hazarika, Peter C. Sercel, Joseph M. Luther, and Jeffrey L. Blackburn**

Supporting Information

Conductivity Tuning via Doping with Electron Donating and Withdrawing Molecules in Perovskite $CsPbI_3$ Nanocrystal Films

E. Ashley Gaulding,[1] Ji Hao,[1] Hyun Suk Kang,[1] Elisa M. Miller,[1] Severin N. Habisreutinger,[1] Qian Zhao,[1,2] Abhijit Hazarika,[1] Peter C. Sercel,[3] Joseph M. Luther,[1,*] and Jeffrey L. Blackburn[1,*]

[1]*National Renewable Energy Laboratory, Golden, Colorado, USA, 80401*
[2]*College of Chemistry, Nankai University, Tianjin 300071, China*
[3] *Department of Applied Physics and Materials Science, California Institute of Technology, Pasadena, California, USA, 91125*

Experimental Section:

Chemicals: All chemicals were used as purchased without further purification unless otherwise noted. Purchased from Sigma-Aldrich: 2,3,5,6-Tetrafluoro-7,7,8,8-tetracyanoquinodimethane (F_4TCNQ, 97%), benzyl viologen dichloride (BV, 97%), Bis(cyclopentadienyl)cobalt(II) (Cobaltocene), sodium borohydride ($NaBH_4$, ≥98%), Cesium carbonate (Cs_2CO_3, 99.9%), oleic acid (OA, technical grade 90%), oleylamine (OAm, technical grade 70%), 1-octadecene (ODE, technical grade 90%), toluene (anhydrous 99.8%), hexane (reagent grade ≥95%), octane (anhydrous, ≥99%), methyl acetate (MeOAc, anhydrous 99.5%), ethanol (EtOH, 200 proof, ≥99.5%)
Purchased from Alfa Aesar: lead (II) iodide (PbI_2, 99.9985%)

NC Synthesis: $CsPbI_3$ nanocrystals (NCs) with individual NC edge-to-edge diameters of ca. 12 nm were synthesized and concentrated in an octane/hexane solution using previously published methods.[1] For most of the films in this work, the temperature of the solution containing PbI_2, ODE, OA, and OAm was raised to 185ºC at the time of injection of the Cs-oleate solution, with a reaction time of 5 sec before quenching in an ice bath. For the optical studies used to monitor the exciton peak during doping (Fig. S1), a more monodisperse NC sample was prepared by injecting at a lower temperature and using size selective precipitation: The PbI_2 solution was raised to 160ºC for the injection of the Cs-oleate. MeOAc was added to the cooled synthesis solution for a total of 50 mL volume and then centrifuged at 7500 rpm for 5 min. The NCs were re-dispersed in ~10 mL of hexane after the supernatant was discarded. Then ~10 mL of MeOAc was added to the NC solution and it was centrifuged at 7500 rpm for 5 min again. The supernatant was transferred to another centrifuge tube and ~15 mL of MeOAc was added to it. The centrifuge process was performed again at 7500 rpm for 5 min. The NC pellet was redispersed in ~3 mL of hexane and then stored in a refrigerator before use.

$CsPbI_3$ NC Film Deposition: 1x1 inch glass substrates (Abs, PL) or 1x2 cm quartz substrates (TRMC) were sonicated in isopropanol then acetone for 10 min each, followed by a 10 min UV-ozone treatment. The following deposition process was done in a flow box kept at ~20% humidity: The NC solution was spin-cast onto the glass substrate at 1000 rpm for 20 sec, then 2000 rpm for 5 sec. The film was then dipped three times in quick succession into dry methyl acetate (MeOAc), which was rapidly dried off

using an N_2 gun. The NC deposition plus MeOAc treatment was repeated three times to build up the film thickness (~ 200-nm).

Fabrication of FET devices: All FET devices were fabricated by utilizing standard optical lithography in the cleanroom. The devices consisted of a p-doped silicon wafer with a 200-nm thickness SiO_2 layer, with electrodes deposited as a 5-nm Ti adhesion layer and an 80-nm Au layer. For deposition onto FET substrates, the concentrated NC solution was diluted 4:1 octane:stock solution and spun at 500 rpm for 20 sec, then 1000 rpm for 10 sec, then rapidly dipped into dry MeOAc three times and blown dry with N_2. This process is done twice (2 layers). The edges of the substrate are then carefully wiped with a q-tip to remove excess NC film and leave just the FET channels covered. Note that this step needs to be done with care as to not damage the electrodes. The Ti adhesion layer is crucial for this reason.

Doping NCs p-type or n-type:

F_4TCNQ Preparation:

A 1.25 mg/mL solution was prepared by dissolving 25 mg of F_4TCNQ in dry toluene in a nitrogen glovebox, resulting in a hazy, dark orange suspension. This was well stirred before used as the source for a series dilution of 0.125, 0.0125, and 0.00125 mg/mL solutions, which were clear with an orange color/tinge.

Benzyl Viologen Preparation:

The neutral BV dopant was prepared by reduction of the BV cation in the benzyl viologen dichloride salt. First, 350 mg of benzyl viologen dichloride was dissolved in 10 mL deionized water; on top of this aqueous solution was layered 10 mL of toluene. This biphasic solution was sealed with a septum and nitrogen was bubbled vigorously through the solution (for at least 10 minutes prior to injection of $NaBH_4$) to purge the solution of oxygen. In a separate vial, 200 mg of $NaBH_4$ was added to 1 mL of deionized water, which creates vigorous bubbling. After allowing this $NaBH_4$ solution to evolve gas for approximately two minutes, the solution was drawn into a syringe and injected into the biphasic benzyl viologen dichloride solution (while nitrogen gas is still bubbling through the BV solution). As $NaBH_4$ induces the two-electron reduction of the viologen salt, the BV turns from clear to blue/violet and migrates into the toluene phase as neutral BV. The reaction is allowed to progress under constant nitrogen bubbling for 10 – 20 minutes. This BV layer in toluene was then drawn into a 20 mL syringe and transferred to a sealed and nitrogen-purged vial that is subsequently pumped into the glovebox. The resulting solution (~3.5 mg/mL BV in toluene) is a deep purple color.

The 3.5 mg/mL stock solution prepared as described above is used as a source for a series dilution resulting in 0.35, 0.035, and 0.0035 mg/mL solutions in toluene.

Doping:

All doping treatments were done in a nitrogen glovebox. NC arrays were doped by immersion of an array in a dopant solution for approximately 5 min (15 sec for cobaltocene as 5 min resulted in a very high resistance/saturation). After removing the array from the dopant solution, it is rinsed by dipping the array into a vial of neat toluene and quickly removing it (ca. 2 sec in toluene). The array was then gently blown dry with an N_2 gun. After doping, the films were kept air free for all measurements using air-free optical

holders (optical measurements), measurement systems inside a glovebox (FTIR, FET, IV, photo-response), or by mounting the sample inside the measurement chamber within a glovebox (TRMC, XPS, UPS).

Fourier transform infrared (FTIR) spectroscopy:

5-nm of Cr as an adhesion layer followed by 100-nm of Au were evaporated onto an Si wafer and cleaved into roughly 5-mm x 5-mm pieces. The NC solution was dropcast onto the substrate and allowed to dry. FTIR measurements were then taken using a Bruker Alpha FTIR spectrometer in diffuse reflectance mode inside an argon atmosphere glovebox. Spectra were collected by averaging between 24 to 128 scans at 2 cm^{-1} resolution. The film was then dipped three times in quick succession into dry MeOAc, which was rapidly dried off using an N_2 gun and the measurement repeated on the same film. The film is then treated with one of the dopant solutions and the measurement repeated again.

Photoelectron spectroscopy (XPS and UPS):

X-ray photoelectron spectroscopy (XPS, hν = 1486.7 eV) and ultraviolet photoelectron spectroscopy (UPS, hν = 21.22 eV) measurements of CPI NCs were performed on a PHI 5600 XPS instrument with an additional UPS arrangement. For the UPS valence band measurements, the pass energy was set to 2.95 eV with a step size of 0.025 eV. The high-resolution core level spectra acquired with XPS had a pass energy of 11.75 eV with a step size of 0.10 eV. The XPS and UPS spectrometer were calibrated with metallic Fermi edges and atomic core levels from Au, Ag, Cu, or Mo. The instrumental response of the XPS and UPS spectrometer is 350 and 180 meV, respectively, and is determined from comparing the measured and calculated Fermi function for a particular instrument condition. The energy uncertainty of XPS and UPS (±0.050 and ±0.025 eV, respectively) is a statistical quantity determined from multiple measurements of the Fermi energy. The NC thin films did have some slight charging, as verified with power-dependent measurements; therefore, the error bars for UPS were increased to ±0.050 eV. The MeOAc treated CPI NC thin films were brought into the XPS/UPS setup through air; however, the doped thin films are brought into the XPS/UPS setup via an air-free configuration.

Absorption:

Absorption measurements were taken on a Varian Cary 5000 in transmission mode in an air-free holder, with baseline correction.

Pump-Probe Spectroscopy:

Transient Absorption:

Transient absorption spectra and dynamics were measured on an Ultrafast Systems system, using the "Helios" configuration, which employs pump and probe pulses with widths of ca. 200 fs and dynamic range for the pump-probe delay of ca. 5 ns. The system is based on a 1 kHz regeneratively amplified Ti:sapphire laser system that produces 4 mL laser pulses at 800 nm. The Ti:sapphire laser pumps an optical parametric amplifier (OPA) to generate the 400 m pump light. The excitation pulse energy employed for exciting the NC arrays was ca. 6.5 nJ at 400 nm (absorbed photon flux of ca. 1.33 x 10^{13} photons·$pulse^{-1}$·cm^{-2}). A portion of the amplified 800 nm light was passed through a sapphire plate to

generate the visible (400 nm < λ_{probe} < 800 nm) continuum probe pulse. The probe pulses were delayed in time with respect to the pump pulse using a motorized translation stage mounted with a retroreflecting mirror. All TA measurements were performed in the air-free optical holder to avoid sample degradation in the presence of oxygen and irradiation.

Time-resolved PL (TRPL):

Time-resolved photoluminescence (TRPL) was measured using a supercontinuum fiber laser (Fianium, SC-450-PP) operating at 10 MHz as the excitation source. The excitation wavelength used was 450 nm, and the pulse energy was approximately 1 nJ. A streak camera for visible detection (Hamamatsu C10910-04) was used to detect time-resolved spectra. The instrument response function (IRF) lifetime was measured to be 260 ps by scattering the excitation beam from the sample, and the time window size was 20 ns. All TRPL spectra were, then, integrated with respect to time to yield steady-state PL.

Flash photolysis Time-resolved Microwave Conductivity (fp-TRMC):

For the TRMC measurements, the CPI nanocrystals were deposited onto quartz substrates (2.5 cm^2 area). The samples are pumped with a 5 ns pulse width beam (650 nm) from an OPO pumped by the third harmonic of an Nd:YAG laser, and probed by microwaves at around 9 GHz. The microwave field is absorbed by photogenerated mobile carriers in the NCs, and its relative change in power ΔP can be measured. The change in microwave power relates to the photoconductivity ΔG through $\Delta P/P = -K\Delta G$ where K is an empirically determined calibration factor for the microwave cavity used in this experiment. The photoconductivity is proportional to the number of charges and their mobility. It can be expressed as $\Delta G = e\beta F_A I_0(\phi\sum\mu)$ where e is the elementary charge, $\beta = 2.2$ is the geometric factor for the X-band waveguide used, I_0 is the incident photon flux, F_A the fraction of light absorbed at the excitation wavelength, ϕ is the quantum efficiency of free carrier generation per photon absorbed and $\sum\mu = \mu_e + \mu_h$ the sum of the mobilities of electrons and holes. Bi-exponential fits of the photoconductivity decay transients were weighted to calculate the average carrier lifetime using the equation: $\tau_{avg} = (A_0\tau_0 + A_1\tau_1)/(A_0 + A_1)$.

FET and photocurrent response measurements:

All FET and photocurrent measurements were performed inside a helium atmosphere glove box with 3 mbar pressure. FET measurement were conducted using two Keithley 2400 source meters: one was used to apply the source-drain voltage (V_{DS}) and monitor the source-drain current (I_{DS}) and the other was used to apply the gate voltage (I_{GS}) and monitor the gate current (I_{GS}). All the experimental parameters and data were controlled and collected by an in house written LabVIEW program. The white light source used for photocurrent response measurement was a white LED array with Dino-lite digital microscope and the 532nm laser was a KOKUYO laser pointer ELP-G30. The power intensity of the 532 nm laser was adjusted by placing a series of neutral density filters purchased from Thorlabs lnc. The spectrum of the white light source was calibrated by Ocean optic USB2000+ portable spectrometer and the power intensity of the white light source and laser pointer were calibrated by using Ophir laser beam profiler purchased from Newport Corporation.

SI Discussion and Figures:

Discussion of Steady State Optical Measurements

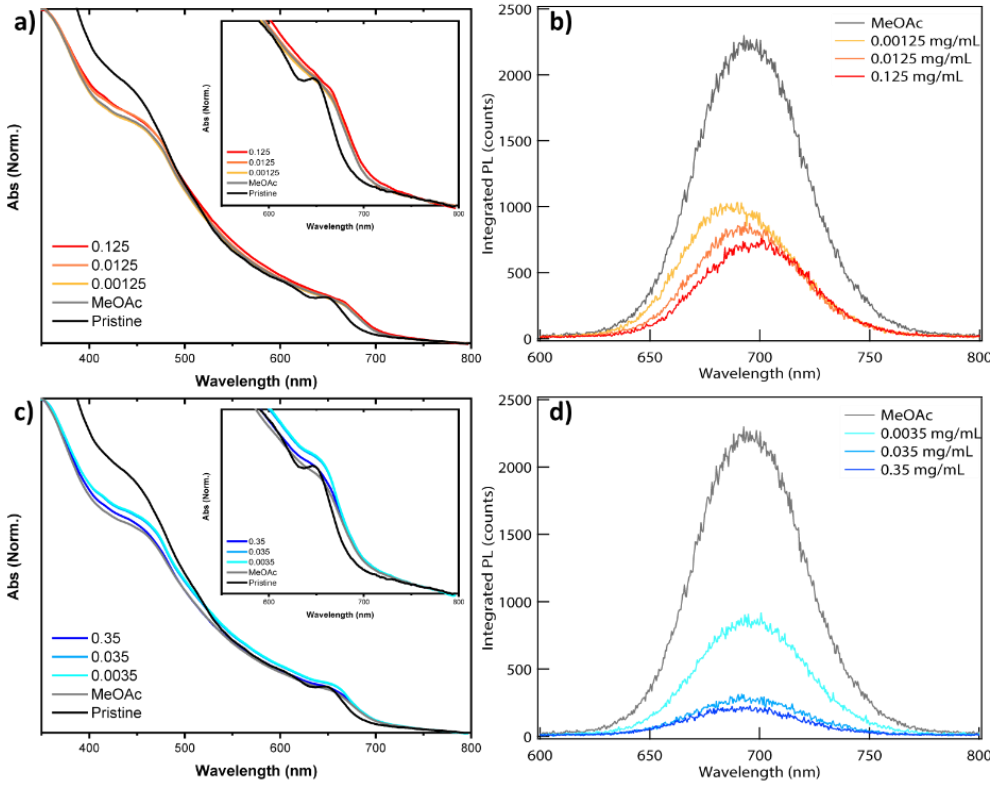

Figure S1: Steady state a) absorption spectra of CPI films with increasing F_4TCNQ doping concentrations (mg/mL). After a significant washing out of the exciton feature after treatment with MeOAc alone, there is little change upon increased doping (inset). b) Concentration dependent PL spectra of F_4TCNQ doped CPI films show an initial blue-shift of the emission peak from MeOAc treatment to lowest doping concentration followed by a progressive red-shift as doping concentration increases. c) Absorption spectra of CPI films with increasing BV doping concentrations. There appears to be some re-definition of the exciton peak with light doping of BV (after initial MeOAc treatment), and a broadening again with the highest doping concentration (inset). d) Concentration dependent PL spectra of BV doped CPI films show a steady decrease of the PL emission intensity, but little shift in the peak position.

Figures S1a and S1c show UV-Vis absorption spectra of two separate arrays that undergo a series of progressive *p*- or *n*-type doping treatments. The undoped array shows characteristic absorption features from a series of excitonic transitions. We find that the ligand exchange process promotes NC coupling and slightly redshifts and broadens the lowest energy excitonic transition. In recent spectro-electrochemical studies by Kamat *et al*., the authors observed rapid and near-total loss of perovskite optical transitions in the absorption spectrum upon negative biasing in spectro-electrochemical experiments.[1] The retention of the optical absorption observed here is an important demonstration that molecular physisorption in the absence of bias is a promising strategy for doping that does not lead to damage of the perovskite structure. Interestingly, none of the molecular doping treatments dramatically

modify the lowest energy excitonic transition, suggesting that the total injected carrier density is relatively low. Moderate to large densities of excess electrons or holes are expected to bleach the lowest energy exciton transition due to phase-space filling.

The photoluminescence spectra shown in Figures S1b and S1d show bright photoluminescence of the untreated array with peak position near 700 nm. Despite the relatively low injected carrier density inferred above, molecular doping causes a decrease in the absolute intensity of emission for both dopants. Interestingly, the electron withdrawing molecule F_4TCNQ causes a small blueshift of up to 20 nm for the emission peak at low surface concentration, which then shifts back to ca. 700 nm at higher dopant concentrations. The addition of excess carriers can affect luminescence quantum yields in a number of ways. The PL quantum yield is related to the relative magnitudes of the radiative recombination rate (k_r) and all other recombination rates (k_{nr}):

$$\phi_{PL} = \frac{k_r}{k_r + k_{nr}} \quad \text{Equation S1}$$

In equation S1, k_{nr} can correspond to any number of non-radiative recombination pathways, including trapping (e.g. Shockley Read Hall), multi-body (Auger-mediated) processes, etc. If mid-gap states are available to trap photo-excited carriers, injected electrons or holes can potentially fill these trap states, eliminating or reducing non-radiative trap-mediated recombination and increasing the quantum yield. However, as discussed above, the general defect tolerance of lead-halide perovskites suggest that most pertinent defect levels do not reside within the gap. Consistently, we do not observe any increase in the PL intensity for the doped NC arrays, even at low doping levels. Since the bi-molecular radiative recombination rate is proportional to the density of electrons and holes, doping in theory could increase k_r and ϕ_{PL} if the excess carriers do not simultaneously increase k_{nr}. However, multi-body Auger-mediated non-radiative processes are known to be enhanced in quantum-confined semiconductors due to spatial confinement of electrons, holes, excitons, and other quasi-particles such as trions and bi-excitons. Such processes involve the non-radiative transfer of energy from the recombining electron and hole to a third particle. Auger-mediated recombination of an electron-hole pair can transfer energy to the third charge carrier, which can be excited into CB or VB states or even ejected from the NC, depending on the available density of states and the corresponding excess energy of the recombining electron-hole pair. The consideration of the DOS for the potential role of Auger-mediated recombination in describing the observed reduction in PL is discussed below.

Discussion of XPS and FTIR chemical signatures

Shown in Figure 1b are the spectra for $CsPbI_3$ NC arrays treated first with MeOAc and then with toluene-based BV or F_4TCNQ dopant solutions. For the FTIR results, the ν(C-H) stretching peaks in the range of 3000 cm^{-1} and ν(C−H_2) at 1466 cm^{-1} suggest that the MeOAc treatment does not completely remove the native oleic acid and oleylamine ligands. Evidence of the individual native ligands used for the NC synthesis can be seen from the broad peak centered at 3138 cm^{-1} which is attributed to stretching vibrations of ammonium groups ν(N−H^{3+}) from starting oleylamine, and symmetric ν_s(COO-) (1409 cm^{-1}) and asymmetric ν_{as}(COO-) (1530 cm^{-1}) stretches from the bound carboxylate group of the starting oleic acid ligand.[2] Absence of a sharp peak from ν(C=O) at 1708 cm^{-1} suggests little or no unbound oleic acid remains in the film after washing of the NCs or with subsequent treatments. Interestingly, the C-H stretching peak intensities are significantly reduced for the BV-doped sample, suggesting that the BV

treatment may remove appreciable amounts of the remaining native ligands. There is some minor reduction of the intensity of the C-H stretching modes near 3000 cm^{-1}, suggesting that the F_4TCNQ treatment may remove small amounts of the native ligands remaining on the NC surfaces following MeOAc treatment. For the XPS results, two chlorine peaks are also observed at binding energies of 199 eV and 200.6 eV (Fig. S3), corresponding to the Cl 2p 3/2 and 2p 1/2 peaks, respectively, suggesting that some amount of chloride anion from the original aqueous benzyl viologen dichloride solution is carried over into the toluene phase used for doping. The entire XPS composition analysis is shown in Table S1 and S2.

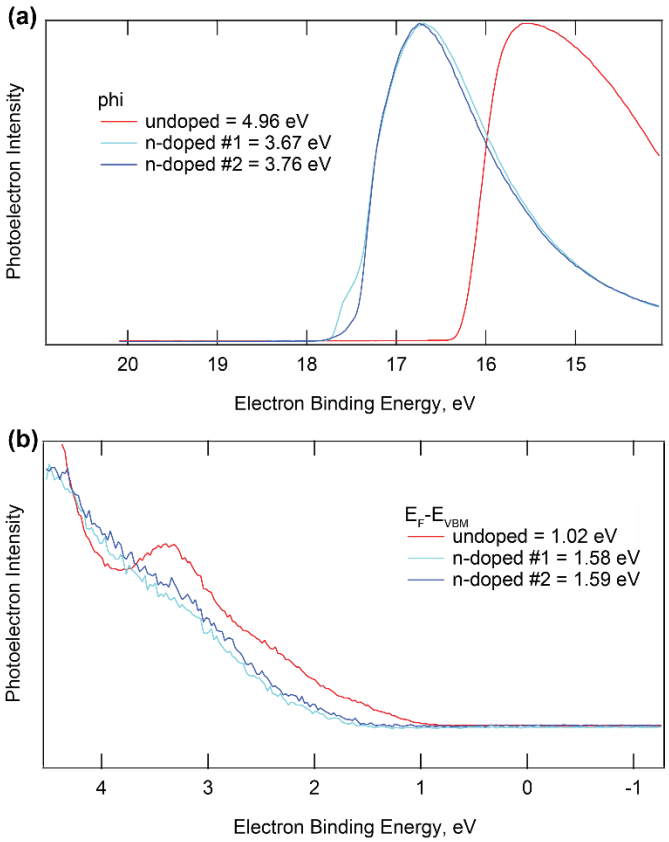

Figure S2: UPS measurements and values for undoped (MeOAc only) and two thin films of n-doped (BV), showing a) the secondary electron cut-off region with extracted workfunction values and b) E_F-E_{VBM} (ionization potential) values. There is a substantial workfunction shift for the BV treated films. The energetics of the F_4TCNQ treated films are not shown because there is apparent desorption of the molecule under transfer to ultra-high vacuum conditions, as is also reflected in the relatively low fluorine signal in the XPS (Figure 1d in the main text).

Energy band diagram calculations:

For Figure 1e, the valence band maximum (VBM or ionization potential) and conduction band minimum (CBM or electron affinity) energies for $CsPbI_3$ are calculated from a combination of the ultraviolet photoelectron spectroscopy (UPS) E_F-E_{VBM} value, UPS workfunction (Φ) value (see Figure S2), and the electronic band gap (measured optical band gap plus an exciton binding energy of 15 meV[3]). The values shown in Figure 1e are an average of UPS measurements taken on multiple undoped $CsPbI_3$ NC films

(Table S2). We note that the measured E_F-E_{VBM} value is an *upper limit* due to the low density of states at the VBM within metal halide perovskite materials.[4] The HOMO and LUMO energies of F_4TCNQ and BV are taken from commonly reported literature values.[5-8]

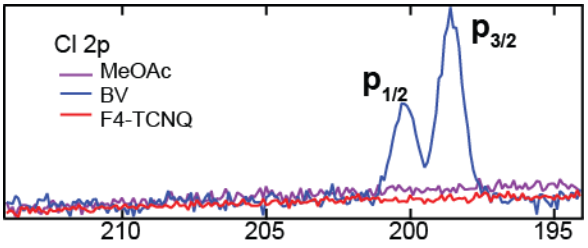

Figure S3: XPS showing the presence of Cl in the BV treated films.

	C	N	O	F	Cl	I	Cs	Pb
Undoped 1	50.85	0	0		0.54	26.89	8.59	10.88
Undoped 2	44.11		1.70			31.70	10.22	11.54
Undoped 3	46.62		2.22			29.70	9.32	11.38
Undoped 4	68.95	2.96	0.79		0.86	16.36	4.08	5.88
Undoped 5	66.16	2.25	0.36		0.38	19.24	4.85	6.70
Undoped 6	56.11	2.65	1.68			22.93	7.02	8.92
#1 n-doped	57.42	2.48	5.05	0.08	6.42	14.18	6.93	7.19
#2 n-doped	54.09	2.22	7.30	0	4.50	16.72	7.25	7.71
#1 p-doped	57.49	0	0	1.36	0.53	24.07	6.86	9.37
#2 p-doped	56.8	0.52	1.26	0.26	0.67	24.07	6.87	9.39

Table S1. Atomic concentrations, extracted from XPS measurements on undoped, p-type, and n-type $CsPbI_3$ arrays.

	Cs:Pb	I:Pb	I:Cs	Φ (eV)	E_F-E_{VBM} (eV)
Undoped 1	0.79	2.47	3.13	4.96	1.02
Undoped 2	0.82	2.75	3.10	4.54	1.21
Undoped 3	0.89	2.61	3.23	4.60	1.20
Undoped 4	0.69	2.78	4.01	4.47	1.31
Undoped 5	0.72	2.87	3.97	4.42	1.33
Undoped 6	0.79	2.57	3.27	4.82	1.00
#1 n-doped	0.96	1.97	2.05	3.67	1.58
#2 n-doped	0.94	2.17	2.31	3.76	1.59
#1 p-doped	0.73	2.57	3.51		
#2 p-doped	0.73	2.56	3.50		

Table S2. Atomic ratios, work functions (Φ) and E_f-E_{VBM} from XPS and UPS measurements.

Discussion of Time-Resolved Spectroscopy

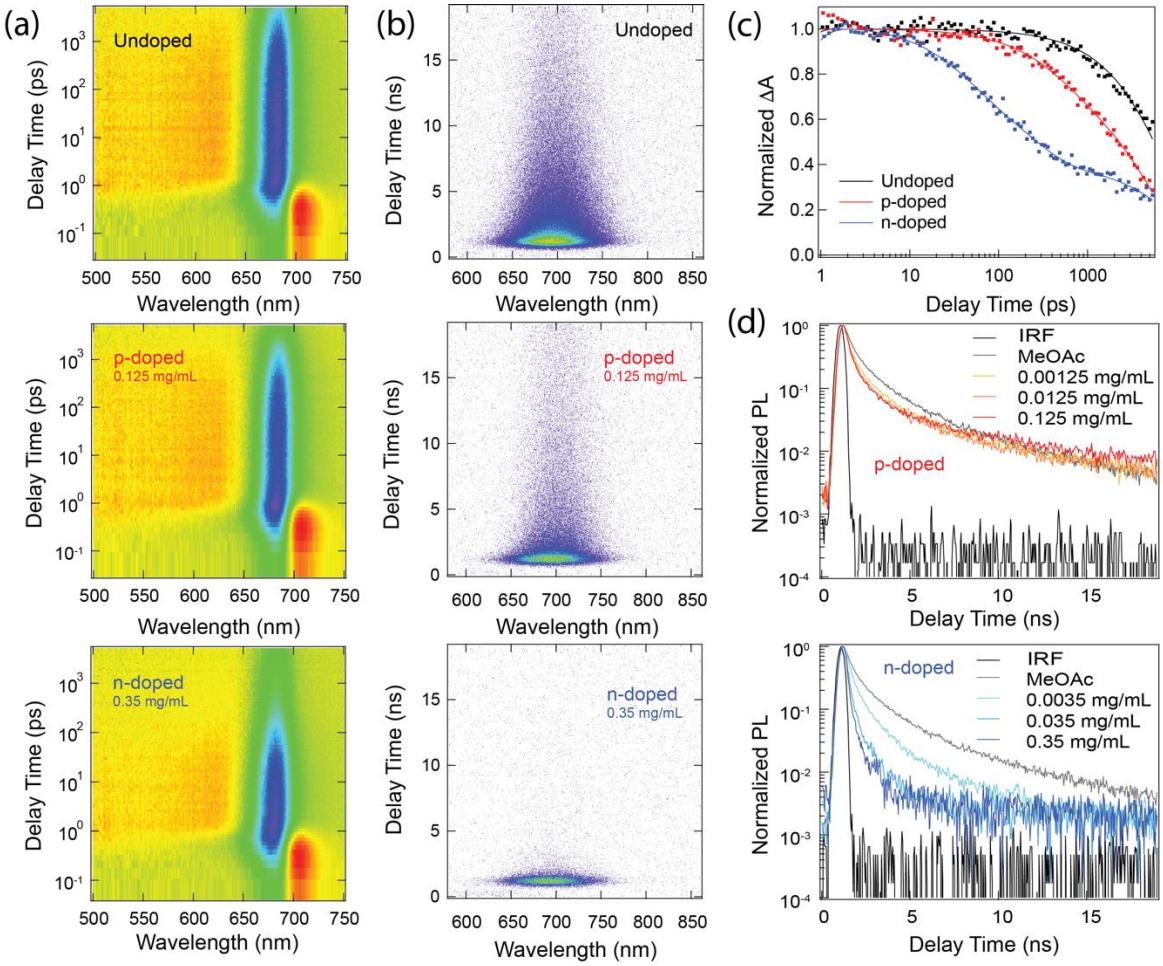

Figure S4. Time-resolved emission and absorption of as-prepared, *p*-type, and *n*-type $CsPbI_3$ NC arrays. (a) Two-dimensional pump-probe transient absorption maps of as-prepared (top), *p*-type (middle), and *n*-type (bottom) $CsPbI_3$ NC arrays. (b) Two-dimensional time-resolved photoluminescence maps of as-prepared (top), *p*-type (middle), and n-type (bottom) $CsPbI_3$ NC arrays. (c) Normalized transient absorption dynamics of the $CsPbI_3$ ground-state bleach (675 nm) for undoped NC array and representative arrays doped *p*-type (F_4TCNQ concentration of 0.125 mg/mL) or n-type (BV concentration of 0.35 mg/mL). (d) TRPL dynamics, taken at the peak of the emission spectrum for a NC array doped *p*-type with progressively increasing concentrations of F_4TCNQ (top) or another array doped *n*-type with progressively increasing concentrations of BV (bottom).

Figure S4a displays two-dimensional TA plots, for undoped $CsPbI_3$ NCs and NCs doped *p*-type or *n*-type with relatively concentrated dopant solutions. The TA measurements are performed at low fluence, to avoid multi-body collisions that can generate trions and biexcitons directly from the pump pulse. The spectral evolution of the TA spectrum is relatively straightforward for all samples. At very early times where the pump and probe pulses are overlapped, the TA spectrum is dominated by a derivative-like feature with positive ΔA at longer wavelengths (red peak $\geq$ 690 nm, Fig. S4a) and negative ΔA at shorter wavelengths (blue peak $\leq$ 690 nm, Fig. S4a). This feature is consistent with the photoinduced Stark effect

observed previously for bulk perovskite materials, whereby the presence of the pump pulse induces an instantaneous bathochromic shift of the ground state absorption. For the remainder of the temporal window (t > 1 ps), the TA spectrum is dominated by a single peak at ca. 683 nm, corresponding to the ground-state bleach (GSB) of the first excitonic transition of the NCs. The dominant effect of both *p*-type and *n*-type doping is the reduction in the lifetime of this GSB, as highlighted by the GSB kinetics displayed in Figure S4c.

Two-dimensional TRPL plots are shown in Figure S4b, and TRPL decays at the peak of the emission envelope are shown in Figure S4d. Similar to the TA results, TRPL measurements demonstrate that both p- and n-type doping lead to reductions in PL lifetime, relative to the undoped NCs.

Discussion of Auger-mediated recombination rates

To better understand the recombination dynamics observed in Figure 2 of the main manuscript and Figure S4, we calculated the band structure of the $CsPbI_3$ NCs. In particular, we wanted to understand the degree to which Auger-mediated recombination may be impacted by the band structure and majority carrier type. We first note that for the doped NCs studied here, we hesitate to assign the observed rapid decay processes specifically to the Auger recombination of *trions*, since (1) our measurements are performed at room temperature, (2) the exciton binding energy (ca. 15 meV)[3] in these NCs is less than *kT* at room temperature, and (3) the NCs are electronically coupled within a film. However, the same basic principles apply to the Auger-mediated recombination of electron-hole pairs in the presence of excess majority carriers. For simplicity, we will use the term *trion* in the following discussion, although such discrete quasi-particles are likely not strongly bound at room temperature in our system at room temperature.

Non-radiative recombination of a trion can occur by an Auger-mediated process whereby an electron and a hole annihilate, with the third carrier present (an electron or a hole in the case of a negative or a positive trion) taking up the energy released by the recombining pair. The rate of decay R_{if} of the trion, initial state *i*, to final state *f*, comprising the excited single remaining carrier, can be calculated using Fermi's golden rule:[9-12]

$$R_{if} = \frac{2\pi}{\hbar} \int |M_{if}|^2 \; g(E_f)\delta(E_f - E_i)dE_f \qquad \text{Equation S2}$$

Here, $g(E_f)$ is the density of final states of energy E_f, for decay of the trion; E_i is the initial energy of the trion, M_{if} is the matrix element for the transition, and the delta function ensures energy conservation. Assuming that the trion is initially in its ground state, energy conservation requires that the final carrier state have energy E_f approximately equal to the band gap energy, E_g, relative to the relevant band edge. That is, the final electron energy will be ~E_g above the conduction band edge in negative trion decay, while the energy of the hole in positive trion decay will be ~- E_g below the valence band edge for the positive trion decay.

The faster Auger-mediated decay observed within n-type versus p-type NC arrays which was discussed in the main text can therefore be conceptually understood by considering the band structure of $CsPbI_3$. Figure S5, panel (a), shows the conduction and valence band structure calculated relative to the R-point of the first Brillouin zone within an 8 band K.P model,[13, 14] while panel (b) shows the corresponding density of states (DOS) calculated from the model band structure. The figure illustrates that the density of final

states available in the Auger-decay of the negative trion (expected in the n-type NC arrays) should be significantly higher than that for the positive trion (expected in p-type arrays). One can see that the negative trion can decay to upper conduction band states that have significantly smaller wave-vector than the corresponding valence band final states involved in positive trion decay. As we will show below this should result in significantly lower probability of Auger decay for the positive trion.

The energy band calculation is made within the Pidgeon-Brown model[13] developed for III-V semiconductors with the modification that the band structure is inverted with respect to that of the III-V and II-VI semiconductors. The valence band has s-like symmetry at the band edge, and is comprised predominantly of Pb 6s and halogen 4p atomic orbitals, with total angular momentum J=1/2.[15, 16] There are 6 p-like conduction bands derived from Pb 6p atomic orbitals and split by spin-orbit coupling into the lowest, 2-fold degenerate conduction band, labelled "near CB" in the figure, characterized by total angular momentum J = ½, and 4 upper J=3/2 conduction bands.[15, 16] In the figure, the band gap is set to the bulk value measured for the cubic phase, E_g = 1.8 eV, while the parameters that determine the band edge effective masses are chosen to be consistent with measured exciton parameters for bulk cubic phase $CsPbI_3$ NCs.[3] The spin-orbit coupling, Δ, separating the lower, J=1/2, and the upper, J=3/2, conduction bands, is taken as Δ = 1.5eV.[16]

In the band diagram shown in Figure S5, panel (a) the positive trion has just one decay path into the excited J=1/2 valence band states at energy E_g below the band edge. By contrast, in this model, for negative trion decay, there are three decay paths: Because $E_g > \Delta$, transitions are permitted not only to excited states in the near J=1/2 CB, but also to the upper J = 3/2, Jz = $\pm 3/2$ and J = 3/2, Jz = $\pm 1/2$ CBs which occur at smaller values of *k*. As a result, all other things being equal, the higher density of final states for negative trion decay would be expected to favor faster decay of negative trions relative to positive trions, in much the same way that CHSH Auger processes (involving excitation from the heavy-hole to the split-off band) dominate in III-V materials where $E_g >$.[9, 12] Moreover, the matrix element for trion decay in NCs has a strong dependence on the crystal momentum of the final state.[10] Analysis of the Auger transition matrix element in small spherical CdS NCs by Chepic et al. demonstrated a $1/k^4$ dependence to matrix element (M_{if} in Eq S-1)[10] which would lead to an additional $1/k^8$ factor in the rate R_{if} favoring processes that connect to final states with small k-values that still conserve energy. The Chepic calculation was made for spherical NCs in the strong confinement regime, for which the NC size is less than the exciton radius, and therefore does not apply to the present situation of cube shaped nanocrystals for which the QD size L > 12 nm, or ~3- 4x the exciton radius.[3] This size range is characteristic of the intermediate confinement regime.[16] An analysis of the problem of Auger-mediated trion decay in this size regime has not yet been undertaken to the best of our knowledge and will be the subject of future work. Nevertheless, a rough estimate of the ratio of the decay rates of the negative to the positive trion was made by assuming the validity of the $1/k^4$ dependence of the matrix element, strictly valid only for strong confinement, and calculating Bloch function overlaps between initial single particle states taken as those of the bulk band edges and plane wave final states, and finally using Eq. S-1. The estimated ratio is in the range 3.5, reflecting the contribution of the two additional upper conduction bands in the decay of the negative trion. While not a rigorous estimate, this is consistent with the ratio of measured decay rates in the n- and p-doped QD arrays studies here.

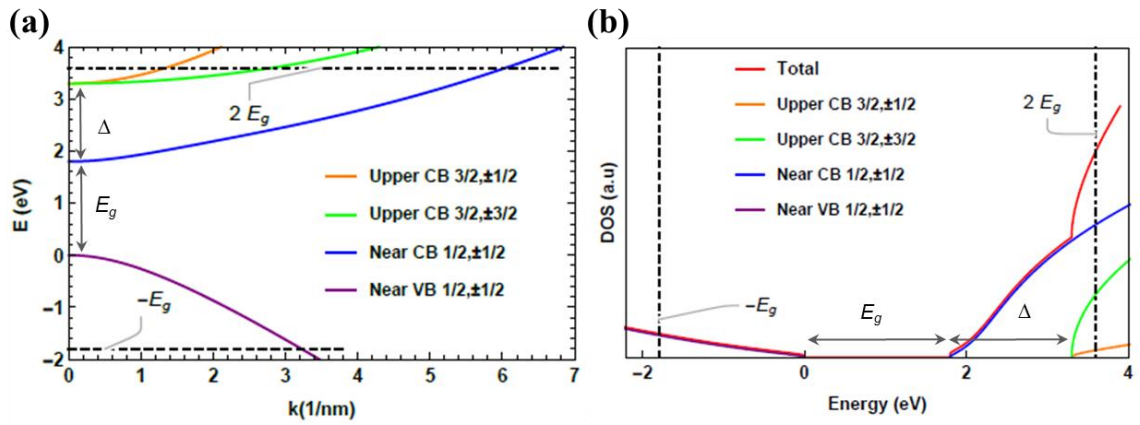

Figure S5: $CsPbI_3$ conduction band and valence band energy band structure, panel (a), and density of states (DOS), panel (b). The band structure in a) was calculated using an 8-band K.P model using band gap, E_g, and effective mass parameters consistent with magneto-exciton measurements in bulk $CsPbI_3$[3] and shows calculated energy versus crystal momentum k relative to the R-point of the first Brillouin zone. In both panels the energy of the final state for positive trion decay is shown as a black dashed line at energy E_g below the valence band edge; the energy of the final state for negative trion decay is shown as a black dot-dashed line. Panel a) shows that for negative trion decay, there are 3 decay channels involving final states at energy $E_f = E_g$ (i.e., E_g above the conduction band edge), respectively in the upper J = 3/2, Jz = $\pm 1/2$ CBs (green line), the upper J = 3/2, Jz = $\pm 3/2$ CBs (orange line) and the near CB with J = 1/2, Jz = $\pm\frac{1}{2}$ (blue line), while positive trion decay proceeds by promoting a hole into a highly excited state within the near J=1/2 VB (purple line) at energy $E_f = -E_g$. Negative trion decay into the J=3/2 upper CBs requires smaller k values than the corresponding decay channels involving either the J=1/2 conduction band (for negative trion decay) or the J=1/2 valence band (for positive trion decay). Panel b) shows the total DOS in red as well as the contributions to the DOS from each individual band. The total DOS at energy $2\,E_g$ represents the density of final states available for negative trion decay, while the total DOS at $-E_g$ is the density of final states for positive trion decay. The plots in the figure were calculated with the following parameters: The band gap, E_g=1.8eV;[3] the spin orbit coupling parameter, Δ = 1.5eV;[16] the Kane energy E_p = 17.4eV, and the conduction band Luttinger parameters γ_1=1 and γ_2 = 0, resulting in band edge effective masses for the electron and hole m_e=m_h = 0.24 of the free electron mass.

Normalized fp-TRMC Transients

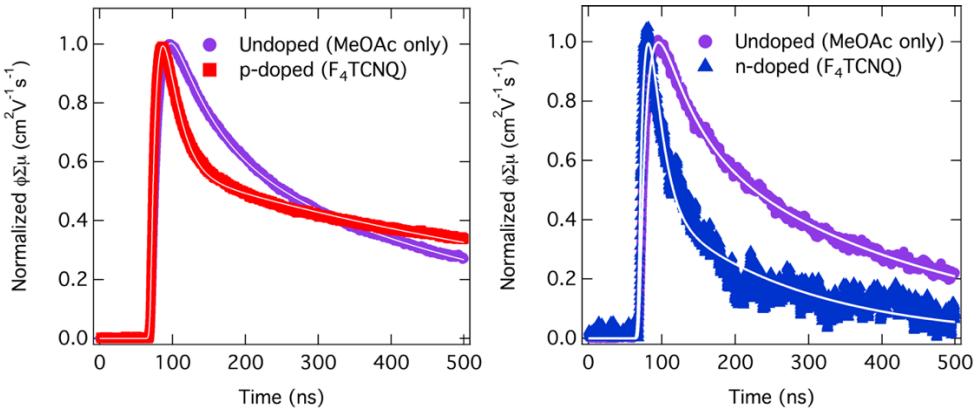

Figure S6: Normalized fp-TRMC curves for comparison of the decay dynamics.

I-V Measurements

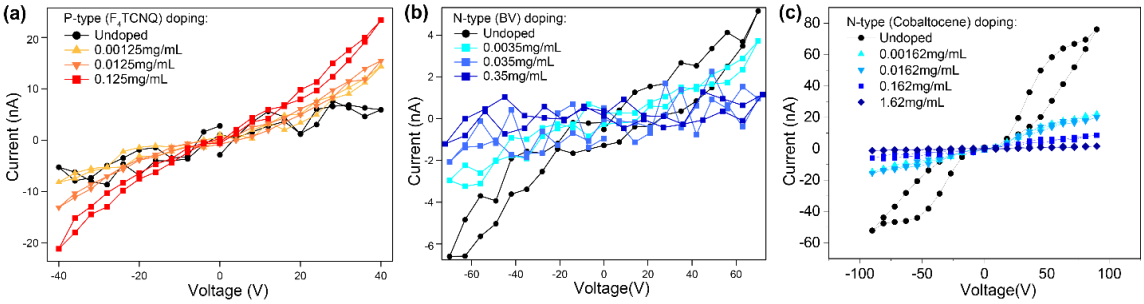

Figure S7. Two-terminal I_{DS} vs V_{DS} I-V curves, measured on a series of $CsPbI_3$ films with increasing dopant concentrations for both molecular dopants. Each panel corresponds to a separate film, where the same film is doped progressively with increasing concentrations of either (a) F_4TCNQ, (b) BV or (c) Cobaltocene.

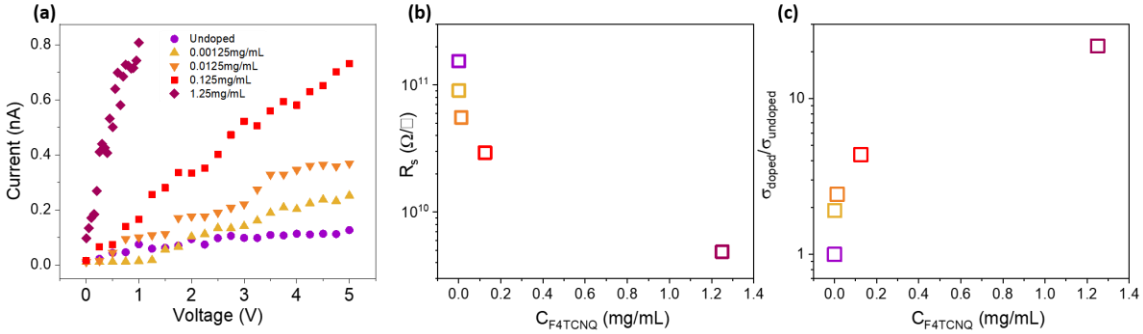

Figure S8. 4-pt probe measurements of F_4TCNQ doped $CsPbI_3$ films showing (a) I-V curves, (b) sheet resistance (Rs), and (c) the conductivity ratio of doped over undoped films as a function of doping concentration.

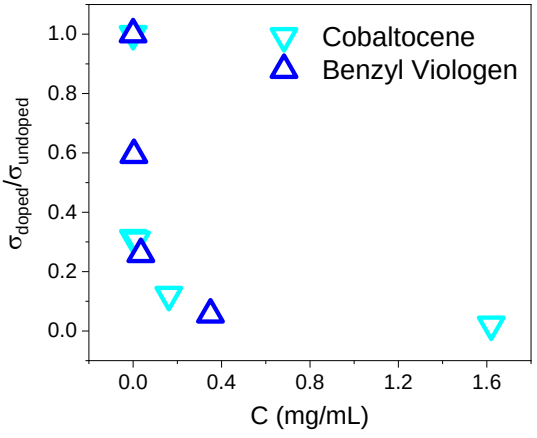

Figure S9: Comparison of conductivity for BV and Cobaltocene as a function of doping density. Both electron donating molecules follow a strikingly similar trend where conductivity shows an inverse relationship to doping concentration.

Photo-response Measurement Setup

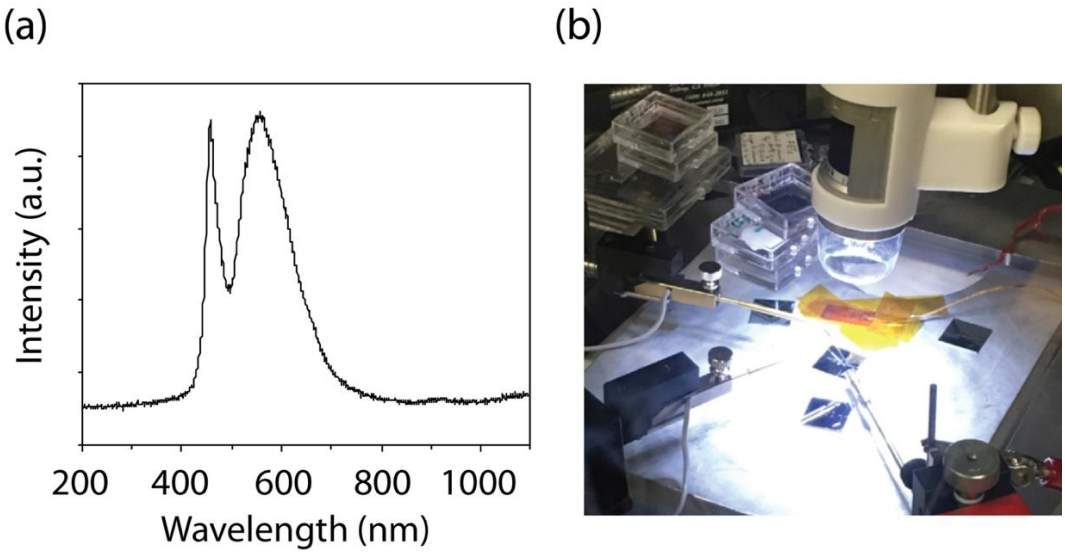

Figure S10. (a) Spectrum of white light LED used to generate low-fluence photo-switching in NC array photo-transistors. (b) Photograph of experimental setup for white light switching of NC array photo-transistors.

References

(1) Samu, G. F.; Scheidt, R. A.; Kamat, P. V.; Janáky, C. Electrochemistry and Spectroelectrochemistry of Lead Halide Perovskite Films: Materials Science Aspects and Boundary Conditions. *Chemistry of Materials* **2018,** *30*, 561-569.
(2) Wheeler, L. M.; Sanehira, E. M.; Marshall, A. R.; Schulz, P.; Suri, M.; Anderson, N. C.; Christians, J. A.; Nordlund, D.; Sokaras, D.; Kroll, T.*, et al.* Targeted Ligand-Exchange Chemistry on Cesium Lead Halide Perovskite Quantum Dots for High-Efficiency Photovoltaics. *Journal of the American Chemical Society* **2018,** *140*, 10504-10513.
(3) Yang, Z.; Surrente, A.; Galkowski, K.; Miyata, A.; Portugall, O.; Sutton, R. J.; Haghighirad, A. A.; Snaith, H. J.; Maude, D. K.; Plochocka, P.*, et al.* Impact of the Halide Cage on the Electronic Properties of Fully Inorganic Cesium Lead Halide Perovskites. *ACS Energy Letters* **2017,** *2*, 1621-1627.
(4) Endres, J.; Egger, D. A.; Kulbak, M.; Kerner, R. A.; Zhao, L.; Silver, S. H.; Hodes, G.; Rand, B. P.; Cahen, D.; Kronik, L.*, et al.* Valence and Conduction Band Densities of States of Metal Halide Perovskites: A Combined Experimental–Theoretical Study. *The Journal of Physical Chemistry Letters* **2016,** *7*, 2722-2729.
(5) Kim, S. M.; Jang, J. H.; Kim, K. K.; Park, H. K.; Bae, J. J.; Yu, W. J.; Lee, I. H.; Kim, G.; Loc, D. D.; Kim, U. J.*, et al.* Reduction-Controlled Viologen in Bisolvent as an Environmentally Stable N-Type Dopant for Carbon Nanotubes. *Journal of the American Chemical Society* **2009,** *131*, 327-331.
(6) Kiriya, D.; Tosun, M.; Zhao, P.; Kang, J. S.; Javey, A. Air-Stable Surface Charge Transfer Doping of Mos2 by Benzyl Viologen. *Journal of the American Chemical Society* **2014,** *136*, 7853-7856.
(7) Liu, D.; Li, Y.; Yuan, J.; Hong, Q.; Shi, G.; Yuan, D.; Wei, J.; Huang, C.; Tang, J.; Fung, M.-K. Improved Performance of Inverted Planar Perovskite Solar Cells with F4-Tcnq Doped Pedot:Pss Hole Transport Layers. *Journal of Materials Chemistry A* **2017,** *5*, 5701-5708.

(8) Li, J.; Zhang, G.; Holm, D. M.; Jacobs, I. E.; Yin, B.; Stroeve, P.; Mascal, M.; Moulé, A. J. Introducing Solubility Control for Improved Organic P-Type Dopants. *Chemistry of Materials* **2015,** *27*, 5765-5774.
(9) Takeshima, M. Auger Recombination in Inas, Gasb, Inp, and Gaas. *Journal of Applied Physics* **1972,** *43*, 4114-4119.
(10) Chepic, D. I.; Efros, A. L.; Ekimov, A. I.; Ivanov, M. G.; Kharchenko, V. A.; Kudriavtsev, I. A.; Yazeva, T. V. Auger Ionization of Semiconductor Quantum Drops in a Glass Matrix. *Journal of Luminescence* **1990,** *47*, 113-127.
(11) Cragg, G. E.; Efros, A. L. Suppression of Auger Processes in Confined Structures. *Nano Letters* **2010,** *10*, 313-317.
(12) Sugimura, A. Band-to-Band Auger Effect in Long Wavelength Multinary Iii-V Alloy Semiconductor Lasers. *IEEE Journal of Quantum Electronics* **1982,** *18*, 352-363.
(13) Pidgeon, C. R.; Brown, R. N. Interband Magneto-Absorption and Faraday Rotation in Insb. *Physical Review* **1966,** *146*, 575-583.
(14) Efros, A. L.; Rosen, M. Quantum Size Level Structure of Narrow-Gap Semiconductor Nanocrystals: Effect of Band Coupling. *Physical Review B* **1998,** *58*, 7120-7135.
(15) Even, J.; Pedesseau, L.; Jancu, J.-M.; Katan, C. Importance of Spin–Orbit Coupling in Hybrid Organic/Inorganic Perovskites for Photovoltaic Applications. *The Journal of Physical Chemistry Letters* **2013,** *4*, 2999-3005.
(16) Becker, M. A.; Vaxenburg, R.; Nedelcu, G.; Sercel, P. C.; Shabaev, A.; Mehl, M. J.; Michopoulos, J. G.; Lambrakos, S. G.; Bernstein, N.; Lyons, J. L*., et al.* Bright Triplet Excitons in Caesium Lead Halide Perovskites. *Nature* **2018,** *553*, 189.